

Article

Synthesis and Use of Silica Xerogels Doped with Iron as a Photocatalyst to Pharmaceuticals Degradation in Water

Cinthia Berenice García-Reyes ^{1,2,*} , Jacob J. Salazar-Rábago ² , Manuel Sánchez Polo ¹ 
and Ventura Castillo Ramos ^{1,*} 

¹ Department of Inorganic Chemistry, Faculty of Science, University of Granada, 18071 Granada, Spain

² Faculty of Chemical Sciences, Universidad Autónoma de Nuevo León, San Nicolás de los Garza 66455, Mexico

* Correspondence: cbgarcia@correo.ugr.es (C.B.G.-R.); vcastillo@ugr.es (V.C.R.)

Abstract: The main objective of this study was to assess the photoactive properties of iron-doped silica xerogels under solar radiation. For this purpose, silica xerogels (XGS) synthesized by the sol-gel method were doped with Fe (III) by two routes: impregnation and polymerization. XGS samples were texturally and chemically characterized by N₂ adsorption, XRD, FTIR, Raman, SEM-EDX, DRS, and PL, evidencing the suitability of using XGS substrates to host iron clusters on their surface with total compatibility. Chlorphenamine (CPM), ciprofloxacin (CIP), and ranitidine (RNT) were used as model compounds. The degradation of the molecules was made under simulated solar radiation testing the synthesis pad, load, material size, and reuse. It was found that XGS doped with Fe by the impregnation route (XGS-Fe-Im) were able to completely degrade CPM and RNT in 30 min and 10 min, respectively, whilst for CIP it achieved the removal of 60% after 1 h of solar radiation exposure, outperforming parent materials and solar radiation by itself. The study of the degradation mechanism elucidated a major influence from the action of HO• radicals. The present investigation offers a potential route of application of XGS Fe-doped materials for the removal of emerging concern contaminants under near real-world conditions.

Keywords: silica xerogels; iron-doped xerogels; photocatalysts; pharmaceutical degradation; water purification; solar photolysis



Citation: García-Reyes, C.B.; Salazar-Rábago, J.J.; Polo, M.S.; Ramos, V.C. Synthesis and Use of Silica Xerogels Doped with Iron as a Photocatalyst to Pharmaceuticals Degradation in Water. *Catalysts* **2022**, *12*, 1341. <https://doi.org/10.3390/catal12111341>

Academic Editors: Paola Calza and Sixto Malato

Received: 29 September 2022

Accepted: 28 October 2022

Published: 2 November 2022

Publisher's Note: MDPI stays neutral with regard to jurisdictional claims in published maps and institutional affiliations.



Copyright: © 2022 by the authors. Licensee MDPI, Basel, Switzerland. This article is an open access article distributed under the terms and conditions of the Creative Commons Attribution (CC BY) license (<https://creativecommons.org/licenses/by/4.0/>).

1. Introduction

Pharmaceuticals are considered emergent pollutants in water; their presence has been detected by several studies over the world [1–3]. The concern about their side effects on the environment and the human population is active although studies on their effects are still being developed [4]. Their removal is essential for maintaining a healthy environment for humans, marine flora, and fauna as their toxicity affects living organisms' normal development and well-being [5–7]. Chlorphenamine (CPM), ranitidine (RNT), and ciprofloxacin (CIP) are active pharmaceuticals present in water effluents in concentrations between 3 and 923 ng/L [8].

Pharmaceutical removal should be done by a technology that is inexpensive, fast, and complete, to achieve the maximal benefits. The main techniques used in the separation of pharmaceuticals from water bodies include adsorption, membrane separation, or the construction of wetlands [9–11]. These treatments do not destroy the drugs and cause additional issues related to the environmental fate of the contaminants. On the other hand, advanced oxidation processes (AOPs) such as ozonation and photocatalytic processes are effective and pose an attractive alternative [12]. They contribute to the efficient degradation of the pharmaceuticals without generating secondary wastes, using relatively inexpensive and inert matrixes with active compounds that could be reused over cycles [13]. Some of the most broadly used photocatalysts for wastewater treatment are TiO₂ and ZnO due to their excellent photocatalytic properties [13,14]. The use of iron in photocatalytic processes has

been widely reported in the literature [15–18] showing high efficacies for organic pollutant removal because of their relatively low redox potential $\text{Fe}^{3+/2+}$ [14].

Silica xerogels are materials obtained through polycondensation, their synthesis is facile and requires very soft conditions [19,20]. Their use as anion adsorbers [19,21], nickel precipitators [22], and sensor supports [23] among many others have been widely reported. Their physicochemical properties (high chemical and mechanical stabilities, ease of functionalization, homogeneous structures, etc., [24]) make them excellent candidates for their use as base materials to host catalytic active substances for their further use in wastewater pharmaceutical photodegradation processes. The functionalization of silica xerogels with catalytically active materials for drug removal, other than titanium dioxide [25,26], is scarcely studied in the literature, being the remediation of tinidazole [14] one of the few reported attempts. Due to their promising prospects, we propose the synthesis of silica xerogels (XGS) doped with iron (III), obtained by facile synthesis as a photocatalyst under simulated solar light. We selected three target pharmaceuticals: chlorphenamine (CPM), ranitidine (RNT), and ciprofloxacin (CIP) to study the potential of our proposed material.

2. Results and Discussion

Several silica xerogels doped with iron (III) were obtained for their use as photocatalysts. Their identifications and synthesis conditions are condensed in Table 1. Several digital photographs are shown in Figure S1.

Table 1. Identification of the synthesized materials and main synthesis conditions.

ID	Synthesis Type	Fe/Si Molar Ratio
XGS	-	-
XGS-Fe-Pol-0.1	Polymerization	1:10
XGS-Fe-Pol-0.3	Polymerization	1:3
XGS-Fe-Im-0.1	Impregnation	1:10
XGS-Fe-Im-0.2	Impregnation	1:5
XGS-Fe-Im-0.4	Impregnation	1:3

2.1. XGS Characterization

The N_2 adsorption isotherm analysis reveals that the materials obtained are predominantly microporous (Table 2), with an average pore diameter of around 1.9 nm and a surface area of around $350 \text{ m}^2/\text{g}$. The materials doped with iron (III) through impregnation showed a decrease of less than 5% in terms of specific area compared to the blank material. A slight decrease in specific area and average pore volume in XGS-Fe-Im with the Fe dose increase can be observed. This indicates the presence of iron lodged in the structure and surface of the support material. Regarding the XGS-Fe-Pol materials, the decrease in surface area and average pore volume was more evident, being 9% against the blank material, this is due to a major “trapping effect” of the iron clusters inside the structure of the base material derived from the polymerization process.

The surface of the materials was examined through SEM (Figure 1). The micrography showed a compact structure of both the blank and the doped XGSs. In all cases, smooth surfaces are presented with continuous fractures resulting from the milling process. It is not possible to observe the formation of metallic clusters, indicating that in all cases the Fe is dispersed through the surface. The EDX surface study confirmed the presence of iron on the surface of the XGSs doped through impregnation, on the other hand, on the materials doped through polymerization iron was only observed in the material with the highest Fe/Si ratio (Figure S2).

Table 2. Textural properties of the different XGSs.

Material	Apparent Surface Area (m ² /g)	Average Pore Diameter (Å)	Pore Volume (cc/g)
XGS	355.1	19.8	0.200
XGS-Fe-Im-0.2	351.0	19.1	0.195
XGS-Fe-Im-0.4	338.1	18.7	0.185
XGS-Fe-Pol-0.3 *	323.4	-	0.149

* CO₂ adsorption isotherm (Dubinin–Radushkevich model).

On the other hand, the XRD analysis, depicted in Figure 2a, shows a wide band in the 2θ angles from 15° to 30° with a maximum signal at 24° corresponding to the amorphous silica, which is present in the three materials. On the other hand, the materials doped with iron showed slight signals at 27°, 35°, 39°, 47°, and 56°. These signals can be associated with the presence of superficial iron in the form of iron oxyhydroxides, specifically from the akageneite (beta-FeOOH) [27]. These diffractions confirm the presence of iron on the surface and demonstrate that it is linked with oxygen atoms, which should be expected considering the precursors and the synthesis route used. The low intensity of the signals can be attributed to a low metal concentration.

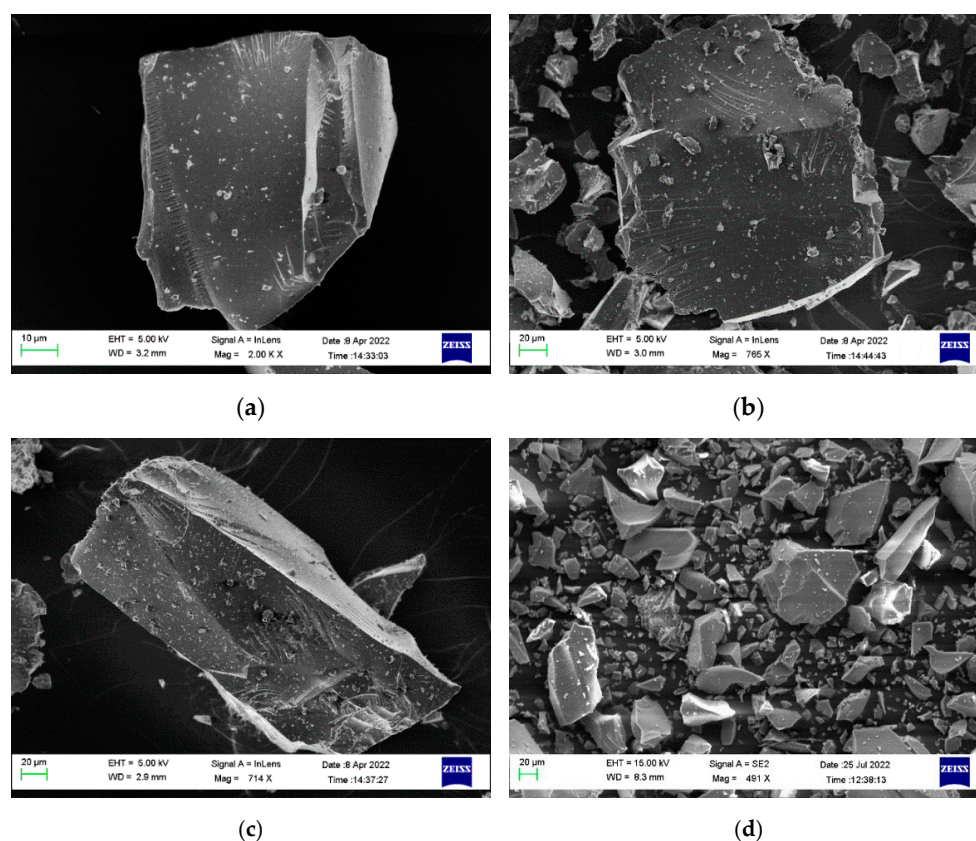


Figure 1. Micrographs obtained for (a) XGS; (b) XGS-Fe-Im-0.4; (c) XGS-Fe-Pol-0.1; and (d) XGS-Fe-Pol-0.3.

The thermal stability of the XGSs was studied using a TGA study, presented in Figure 2b. XGS showed a 12% mass loss at 110 °C, while XGS-Fe-Im-0.4 and XGS-Fe-Pol-0.1 showed a 19% mass loss at the same temperature, this weight loss is associated with a loss of humidity and leftover components from the synthesis process. The materials containing iron could have a greater loss due to a higher quantity of residuals from the synthesis since they may be captured in the step to incorporate the metal. The XGS-Fe materials show great thermal stability, losing weight gradually up until a maximum of 20% when

the temperature increases to 900 °C. The thermal decomposition curves of the Fe-doped materials showed a profile similar to XGS weight loss, indicative of the total compatibility and adequation of the use of these types of materials to host iron.

The FTIR study, Figure 2c, of XGS achieved the identification of the Si-OH groups from their characteristic stretching band at 790 cm^{-1} , on the other part, the Si-O-Si bands were identified at 450, 930, and 1045 cm^{-1} corresponding to the stretch (symmetric and asymmetric) and bending movements [19,28]. This technique did not allow to appreciate differences between the spectra of the blank and Fe-doped materials, since the Fe-O signals are usually around 880–860 cm^{-1} and can be eclipsed by the silanol group bands.

The Raman spectra in Figure 2d show the iron present in the XGS-Fe-Im materials related to the bands at 331 and 720 cm^{-1} [29] with the most intense band being the one corresponding to the sample with the highest amount of Fe. By contrast, the metal presence in the XGS-Fe-Pol material is only evident in the sample with the highest Fe concentration, the band does not appear in the material with the lowest metal concentration. Higher concentrations of the metallic precursor during the polymerization process increase the probability of the material homogeneously coating the surface of the support material, meanwhile, at low concentrations, the metallic clusters remain entrapped inside the xerogel's matrix. There is no evident appearance or shift of other bands in the spectra of the materials after the metal incorporation, once again showing the lack of a chemical reaction between the silicon matrix and the iron, being both completely compatible.

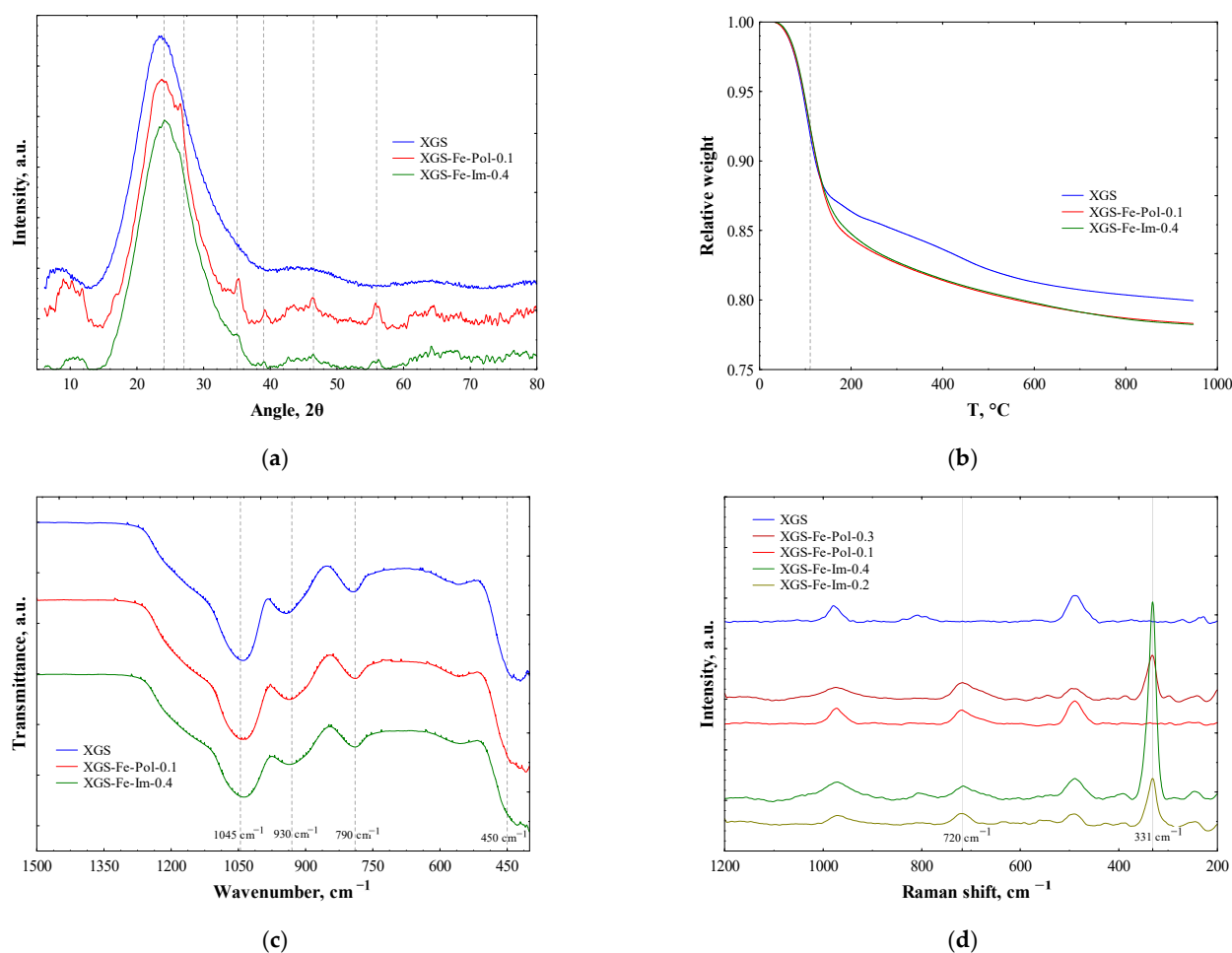


Figure 2. Surface characterization for XGS and the ones doped with iron: XGS-Fe-Im and XGS-Fe-Pol. (a) XRD; (b) TGA; (c) FTIR; and (d) Raman spectra.

The surface chemical composition percentages of the synthesized materials were obtained through XPS (Table 3). The minor quantities of carbon, nitrogen, and chlorine come from the reagents used during the synthesis process. As expected, the predominant elements are silicon and oxygen, it can also be observed that in most cases, the O/Si ratio stayed at 2.5, which showed that the adhesion of iron did not affect these bonds. Moreover, the metallic ion's presence was quantified for the materials doped. By analyzing the elemental O/Fe ratio, it decayed in the following order: XGS-Fe-Pol-0.3 > XGS-Fe-Im-0.4 > XGS-Fe-Im-0.2, which can be associated with the degree of linking between the iron and oxygen atoms in the surface of the material.

Table 3. Chemical composition of the surface obtained by XPS analysis, all quantities in percentage.

Material	O 1s	Si 2p	Fe 2p	C 1s	N 1s	Cl 2p
XGS	67.72	27.12	-	5.00	0.16	-
XGS-Fe-Pol-0.3	59.05	23.97	1.42	14.10	0.29	1.18
XGS-Fe-Im-0.2	57.66	19.19	3.96	15.89	0.41	2.90
XGS-Fe-Im-0.4	55.24	21.88	2.65	16.67	0.55	3.01
XGS-Fe-Im-0.2-O	59.82	20.87	3.10	15.20	0.37	0.64
XGS-Fe-Im-0.4-O	62.46	24.01	1.45	11.32	0.47	0.28

* Final -O stands for outworn materials.

Figure 3 shows the high-resolution spectra for silicon and iron for XGS and XGS-Fe-Im-0.2. Both materials show a Si 2p signal between 102 and 106 eV. Several authors have reported that in this energy interval the Si-OH, Si-O-Si, and Si-O-Fe can be found at 103.6, 103.1, and 101.9 eV respectively, which is to be expected for the materials synthesized [30]. When comparing the spectra of both materials, no significant change in shape can be observed, this can be due to the low iron content in relation to the Si and O contents, since for the Im-0.2 material the Si/Fe ratio is 4.9. The high-resolution spectra for other materials can be found in the Supplementary material (Figure S3).

Concerning the Fe 2p spectra, XGS does not show a signal for the iron element as expected. On the other hand, for XGS-Fe-Im-0.2 the signal doublet attributed to the iron 2p can be observed at 724.5 and 711 eV, these correspond to the Fe 2p 1/2 and Fe 2p 3/2 regions respectively. In the Fe 2p 3/2 region it has been reported that the iron can present itself to bond to oxygen in the following forms: Fe₂O₃, and FeO(OH) at 711 and 713 eV, respectively, the first interaction indicates that it is bonded with oxygen and that its oxidation state is Fe⁺³ [14]. Similar results were observed for XGS-Fe-Im-0.4 and XGS-Fe-Pol-0.3 (Figure S3).

Together, the results from XRD, SEM-EDX, Raman spectroscopy, and XPS provide important evidence of the presence of iron on the surface of the XGS-Fe materials.

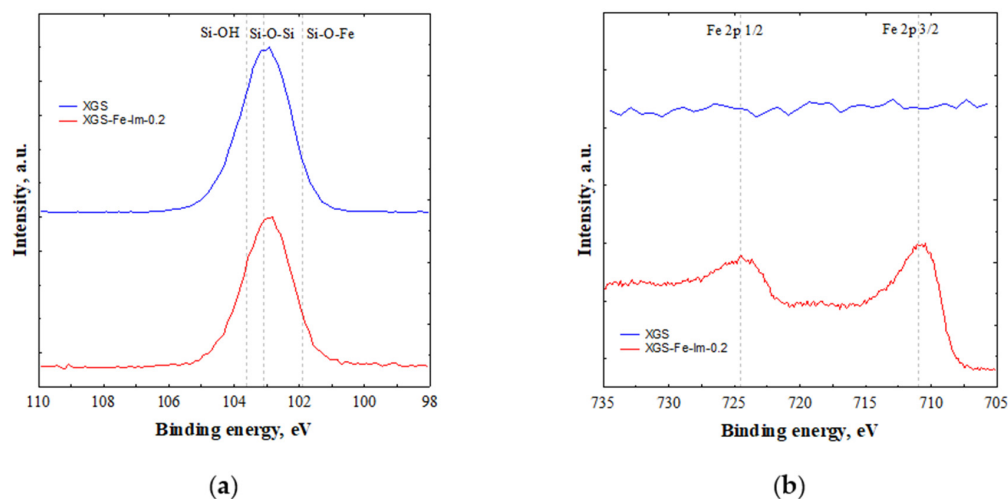


Figure 3. High-resolution XPS spectra for XGS and XGS-Fe-Im-0.2 (a) Si 2p; and (b) Fe 2p.

The band gap energy for the materials was calculated using the Kubelka–Munk function [14]. For XGS, a value of 4.25 eV was obtained, meanwhile, values of 2.95 and 3.05 eV were observed for XGS-Fe-Pol-0.3 and 0.1 respectively. Likewise, values of 3.03 and 3.08 eV were obtained for XGS-Fe-Im-0.2 and 0.4 (Figure 4). In this sense, the materials doped with iron are active in the electromagnetic spectrum's visible region starting in the range between 402 and 420 nm.

On the other hand, the photoluminescence studies (Figure S4) showed that the metal presence decreased the emission intensity, meaning that it extends the half-life period of the electron-hole pair. It was also revealed that the XGS-Fe-Im materials show a larger decrease when comparing them to the XGS-Fe-Pol materials.

Both results are relevant to understand the performance of a photocatalyst.

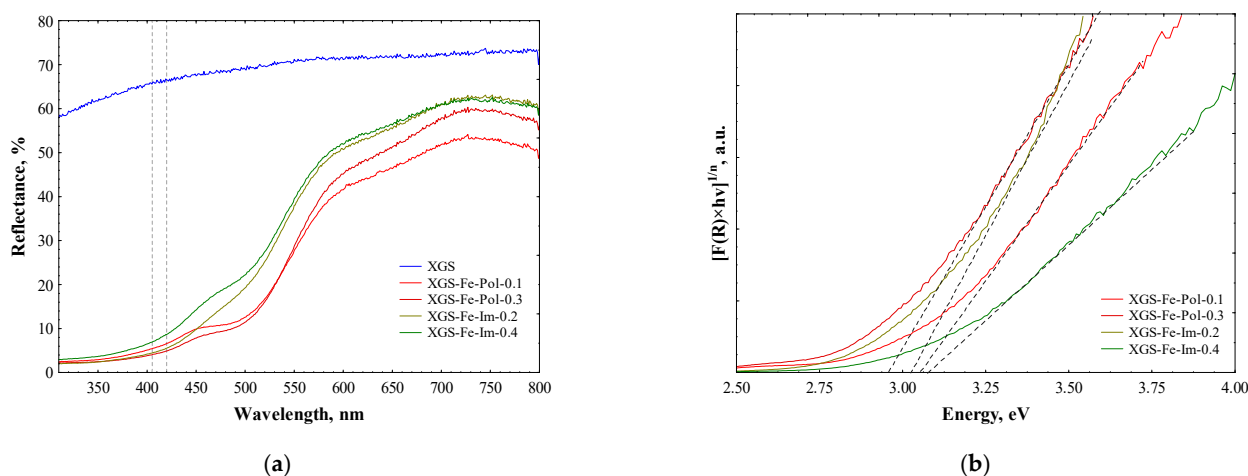


Figure 4. Photoelectronic characterization of the XGSs. (a) Diffuse reflectance spectra; and (b) Kubelka–Munk graphic for the determination of the band gap energy.

2.2. CPM Degradation

The CPM's degradation kinetics performed under solar radiation are shown in Figure 5. It is worth noting that adsorption was measured and resulted null during 30 min before the start of radiation in all experiments performed. CPM molecule showed great stability since the degradation by direct photolysis after 60 min of exposure was only 12%. The presence of XGS did not improve this result, achieving the same 12%. Regarding the iron-doped materials, a load of 1 g/L of XGS-Fe-Pol-0.3 achieved a 12% CPM degradation, meaning that there was no benefit with respect to solar photolysis. On the other hand, the pharmaceutical compound is completely degraded in 30 min of irradiation with the presence of XGS-Fe-Im-0.4, which was doped through impregnation.

Although the textural characterization did not show significant differences between materials doped through impregnation from the ones doped through polymerization, a difference in the amount of surface iron could be observed. The presence of surface iron is relevant for the photocatalytic process since it allows the photons to achieve the activation of the material and the formation of oxidant species; having the material doped through impregnation with a larger quantity of surface iron than the one doped through polymerization allows a bigger possibility of forming said oxidant species. This, along with the half-life times of the electron-hole pair, which the PL results suggest is larger for the XGS-Fe-Im materials, increases the possibilities of forming the aforementioned oxidant species, which explains the results obtained. The next section of the study was focused on XGS-Fe-Im materials, dismissing XGS-Fe-Pol materials as photocatalysts.

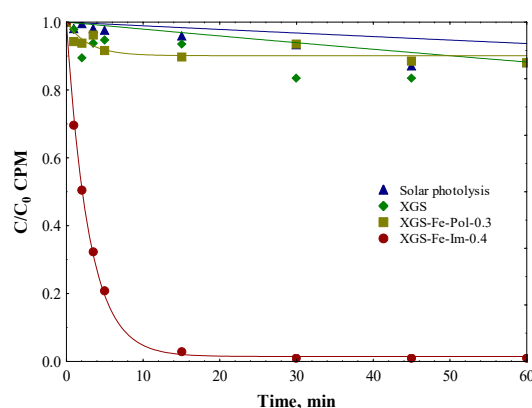


Figure 5. CPM's degradation under direct solar radiation or in the presence of XGS, XGS-Fe-Pol-0.3, or XGS-Fe-Im-0.4. Load of 1 g/L, $C_0 = 15$ ppm.

Table 4 enlists the experiments performed, as well as the kinetic constants obtained for the first-order model and the two-parameter first-order model, this model has been reported for the fitting of experimental data in heterogeneous photocatalytic processes [31]. It can be observed that, for the materials obtained through impregnation, the two-parameter first-order model fitted the experimental data better, achieving lower deviation percentages than those obtained by the first-order model. Therefore the 2-parameter model's representation is the one used in the graphs presented in this study.

Table 4. List of experiments and kinetic constants obtained along with the deviation percentage.

Pollutant	Material	Load, g/L	k_1 (min^{-1})	%D	k_2 (min^{-1})	β_A	%D
CPM	-	-	0.001	3%	-	-	-
CPM	XGS	1	0.002	5%	0.139	0.856	2%
CPM	XGS-Fe-Pol-0.1	1	0.001	2%	0.020	0.945	2%
CPM	XGS-Fe-Pol-0.3	1	0.003	4%	0.350	0.901	2%
CPM	XGS-Fe-Im-0.1	1	0.007	2%	0.024	0.611	1%
CPM	XGS-Fe-Im-0.2	0.5	0.195	32%	0.206	0.026	31%
CPM	XGS-Fe-Im-0.2	1	0.323	42%	0.332	0.015	24%
CPM	XGS-Fe-Im-0.2-M	1	0.065	10%	0.085	0.096	7%
CPM	XGS-Fe-Im-0.2-L	1	0.125	9%	0.142	0.054	7%
CPM	XGS-Fe-Im-0.2	1.5	0.359	13%	0.361	0.003	9%
CPM	XGS-Fe-Im-0.4	0.5	0.317	27%	0.324	0.010	13%
CPM	XGS-Fe-Im-0.4	1	0.330	43%	0.340	0.015	22%
CPM	XGS-Fe-Im-0.4	1.5	0.367	2%	0.366	0.000	2%
CPM	XGS-Fe-Im-0.4-tBuOH	1	0.006	4%	0.213	0.873	2%
CPM	XGS-Fe-Im-0.4-NO ³⁻	1	0.349	16%	0.350	0.007	11%
CPM	XGS-Fe-Im-0.4-Thiourea	1	0.001	2%	0.330	0.956	0%
CPM	XGS-Fe-Im-0.2-O	0.5	0.005	4%	0.075	0.789	3%
CPM	XGS-Fe-Im-0.4-O	1	0.004	2%	0.007	0.326	1%
CPM	XGS-Fe-Im-0.4-O	1.5	0.009	5%	0.011	0.172	5%
RNT	-	-	0.125	11%	-	-	-
RNT	XGS-Fe-Im-0.2	1	0.336	47%	0.390	0.069	10%
RNT	XGS-Fe-Im-0.4	1	0.465	49%	0.544	0.066	5%
CIP	-	-	0.029	12%	-	-	-
CIP	XGS-Fe-Im-0.2	1	0.020	5%	0.043	0.325	3%
CIP	XGS-Fe-Im-0.4	1	0.015	7%	0.068	0.508	5%

* Final -M and -L stands for the size of the particles, and final -O stands for outworn materials.

The effect of iron concentration through impregnation on CPM's degradation kinetics was analyzed (Figure 6a). For XGS-Fe-Im-0.1, a first-order kinetic constant of 0.007 min^{-1} was observed, meanwhile, the constants for XGS-Fe-Im-0.2 and 0.4 were 0.323 and 0.330 min^{-1} respectively. Therefore, it was decided to deepen the study of these two materials.

The similarity in their velocities can be explained by the quantity of surface iron found in the XPS study, where a minor variation was found between both.

The effect of particle diameter was studied for XGS-Fe-Im-0.2 (Figure 6b), where the kinetic constant was favored as the particle diameter decreased. In terms of degradation percentages with time, it can be appreciated that at 60 min of treatment the biggest difference observed was only 6%. These results can be correlated to the fact that a bigger particle size means less surface in contact with the aqueous medium and to a screening or photon-blocking effect that delays the degradation process.

The effect of material load (Figure 6c,d) demonstrated that there is an increase in the kinetic constant when the load increases from 0.5 to 1.5 g/L in both materials, being more notable in XGS-Fe-Im-0.2, where the kinetic constant incremented by 46% with the load increase, however, the most significant change was observed in the rise from 0.5 g/L to 1.0 g/L for this material. With XGS-Fe-Im 0.4, the kinetic constant increased only by 13% when the load of the material increased three-fold (from 0.5 to 1.5 g/L).

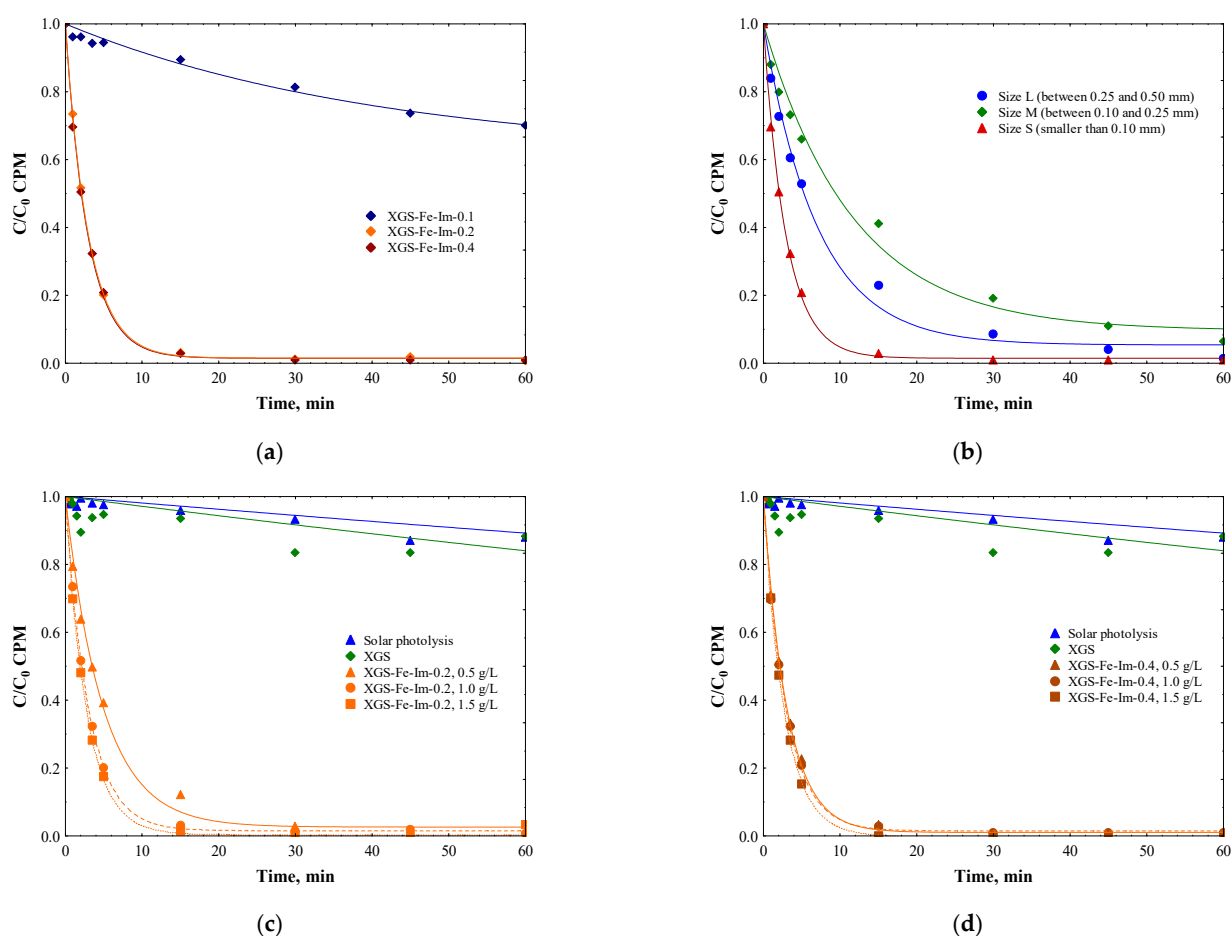


Figure 6. Studies on the XGSs in CPM degradation, in all cases $C_0 = 15$ ppm: (a) effect of impregnation rate during synthesis; (b) effect of the particle diameter with XGS-Fe-Im-0.2 material; (c,d) effect of the material load for either XGS-Fe-Im-0.2 and 0.4.

Few authors have performed CPM degradation. Wang et al. [32] worked in dark with zero-valent iron particles, at pH 3 and added 0.1 mL of H_2O_2 achieving a kinetic constant of 0.059 min^{-1} . On the other hand, Mar-Ortiz et al. [33], using a carbon xerogel with iron at pH 3 and under visible light, observed kinetic constants from 0.092 min^{-1} to 0.420 min^{-1} , the higher value due to the addition of H_2O_2 .

To analyze the degradation mechanism, the electronic properties of the XGSs were calculated. For this, the data obtained by XPS in an interval of 0 to 7 eV was used to

estimate the valence band (E_{VB}), as reported by several authors [34–37]. The value of the conduction band (E_{CB}) was estimated by subtracting the value of the band gap from the E_{VB} ($E_{VB} = E_{CB} - E_g$) [38]. It is known that the redox potential of $HO\bullet/OH^-$ is 1.99 eV and that of $O_2/O_2\bullet^-$ is -0.046 eV [34]. As depicted in Figure 7a, and Figure S5, XGS-Fe-Im has a working potential including both values, therefore it is likely that the material could act through these pathways.

To complement the previous results, several electron and hole-trapping molecules were used during the experiments to clarify the relevance of several radical species (Figure 7b and Table 4). The presence of NO_3^- ions increased the value of the kinetic degradation constant by 5.8%. Other studies have observed an increase in the kinetic constants due to the presence of NO_3^- since it promotes the $HO\bullet$ radical formation in irradiations waves higher than 280 nm [39]. Meanwhile, thiourea and tert-butanol inhibited the photocatalytic process, so it is proposed that CPM's degradation occurs mainly through the formation of $HO\bullet$ radicals (Table 4) [31].

Consequently, we propose that XGS-Fe-Im-0.4 promotes the formation of hydroxyl radicals, through the reaction of the hole with OH^- anions, which play the main role in the degradation of pharmaceutical compounds.

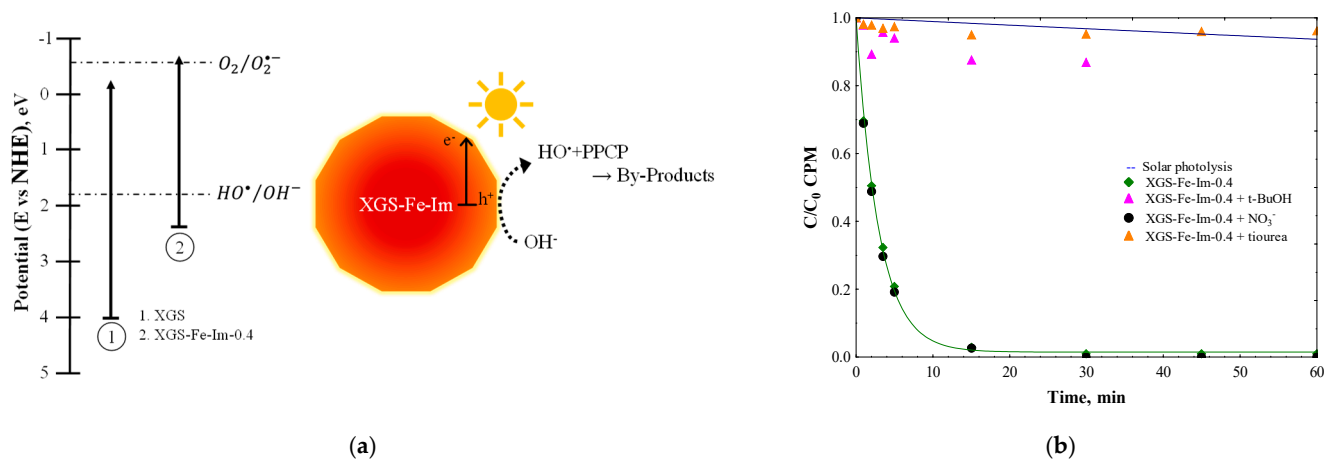


Figure 7. (a) Band structure of XGS and XGS-Fe-Im-0.4; (b) CPM degradation mechanism study using XGS-Fe-Im-0.4 and several scavengers. $C_0 = 15$ ppm.

XGS-Fe-Im-0.2 and 0.4 were tested in a reuse cycle where a decrease in the degradation rate of 97% and 99% was observed (Figure 8a and Table 4). Given these results, iron analyses were performed in the solution. A metal lixiviation phenomenon was evident for both materials, it is notably superior for XGS-Fe-Im-0.4, about 5.3 times than XGS-Fe-Im-0.2 (Table S1). It is interesting to note that iron lixiviation is increased after solar radiation when compared to the solution kept in dark, by 1.6 and 4.9 times for XGS-Fe-Im-0.2 and 0.4, respectively. Moreover, the characterization of the outworn materials demonstrated a decrease in surface iron (Table 3 and Figure S6), as well as an increase in the photoluminescence emission (Figure 8b). This confirms that the outworn material loses its effectivity due to a drop of surface iron and because the electron-hole pair has a faster recombination time, it has fewer possibilities of generating oxidating species for the degradation of the contaminant. The loss of surface iron can be due to a self-attack from the radicals generated by the irradiation in the polymeric matrix, allowing the liberation of the iron. The decrease in the effectivity of the material during a reuse cycle indicates that it is a hydroxyl radical promoter, rather than a photocatalyst.

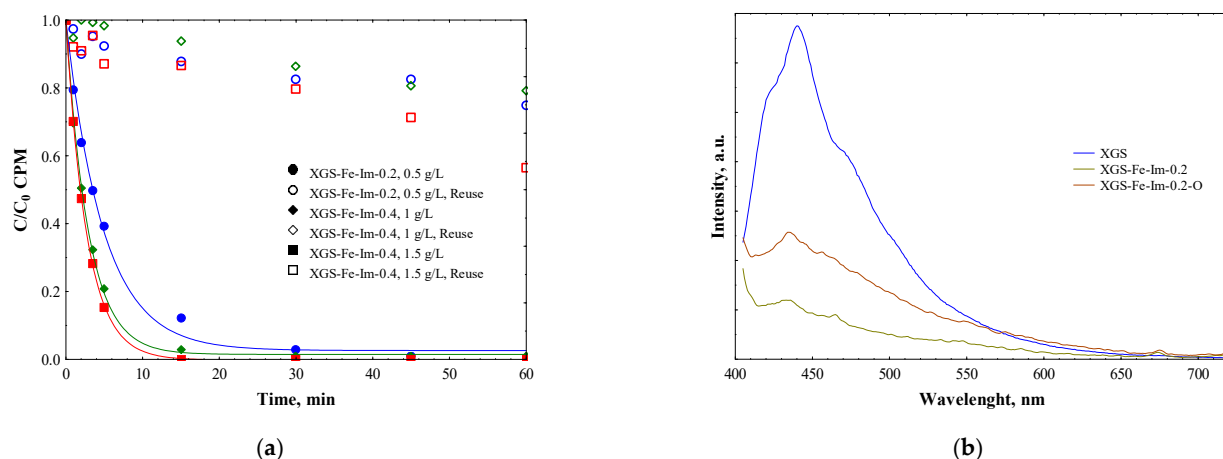


Figure 8. (a) CPM's degradation curves for several reuse tests for the XGSs materials. $C_0 = 15$ ppm. (b) Photoluminescence emission spectra for XGS-Fe-Im-0.2 and the outworn material.

2.3. RNT and CIP Degradation

Likewise, the materials were tested for the degradation of other pharmaceuticals of interest, RNT and CIP (Figure 9 and Table 4). RNT's degradation showed kinetic constants of 0.336 and 0.465 min^{-1} , with XGS-Fe-Im-0.2 and 0.4 respectively, while the degradation percentages at 15 min were the same between the two materials. There are scarce reports on RNT degradation by photocatalysis. Radjenovic et al. [40] used a pilot plant with a CPC, using two processes, heterogeneous photocatalysis with TiO_2 , and photo-Fenton, they report a kinetic constant of 0.146 and 0.23 min^{-1} , respectively on RNT degradation. Zou et al. [41] develop MoS_2/RGO composites, achieving a kinetic constant of 0.021 min^{-1} under visible light.

On the other hand, for the degradation of CIP, kinetic constants of 0.02 and 0.015 min^{-1} were obtained for XGS-Fe-Im-0.2 and 0.4 materials respectively. It has been reported by Zheng et al. [42] the use of TiO_2 and a composite graphitized with TiO_2 under UV light to achieve a kinetic constant of 0.102 min^{-1} , and 0.107 min^{-1} , respectively. On other hand, Núñez-Salas et al. [43] achieved a kinetic constant of 0.041 min^{-1} under UV-Vis radiation by using a new composite $\text{FeTiO}_3/\text{ZnO}$.

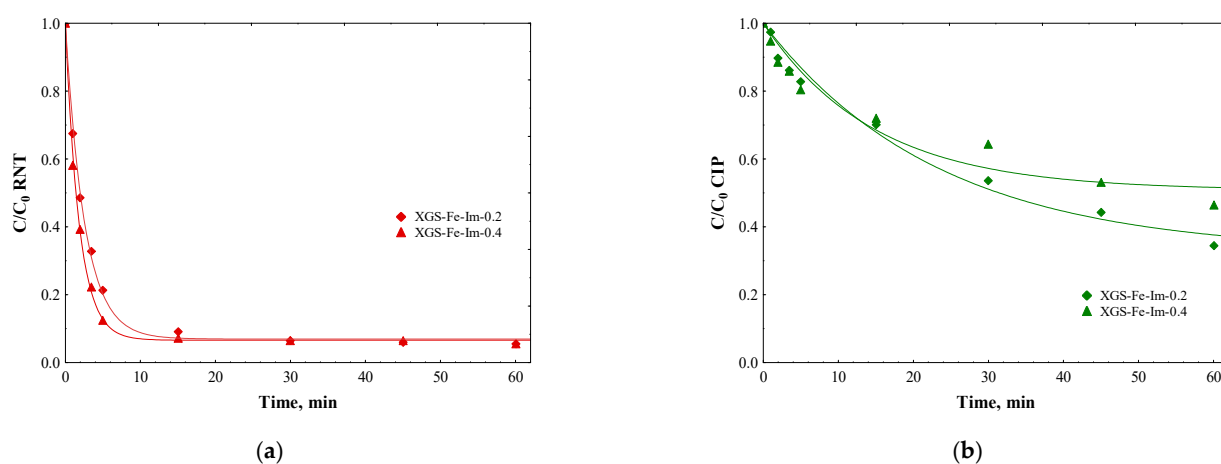


Figure 9. Degradation curves using XGS materials with a load of 1 g/L and $C_0 = 15$ ppm (a) RNT (b) CIP.

The kinetic constants obtained reveal a decrease in the magnitude in the order $\text{RNT} > \text{CPM} > \text{CIP}$, which can be attributed to the structural complexity of the molecules, where the RNT is the least complex molecule with just one cyclic ring and a semi-linear configuration.

On the other hand, CPM presents two separated aromatic rings whereas CIP presents two fused aromatic structures with bonds in resonance which decreases the effectivity of the radical attack and subsequent degradation [44].

The degradation achieved with XGS-Fe-Im-0.2 and 0.4 for three studied compounds, CPM, RNT, and CIP, proved to be comparable to other studies on CPM and RNT degradation, with the advantage that no pH adjustment was made, or no additional reagent was required.

3. Materials and Methods

3.1. Reactants

Chlorphenamine (CPM), ranitidine hydrochloride (RNT), and ciprofloxacin hydrochloride (CIP) were acquired from Sigma-Aldrich high-purity grade, ammonium hydroxide (NH_4OH), hexahydrate iron (III) chloride (FeCl_3), and formic acid (HCOOH) were acquired from the same company. The reactants: 37% hydrochloric acid (HCl) and 2-propanol ($\text{C}_3\text{H}_8\text{O}$, iPrOH) were obtained from PanReac AppliChem (ITW Reagents, Barcelona, Spain). On the other hand, tetraethyl orthosilicate (TEOS) from the ACROS Organics brand was used, and HPLC-UV grade acetonitrile and methanol were used from the Scharlau brand. The water used in the solutions was of bi-distilled water (DW) quality obtained from a Millipore equipment (Milli-Q Synthesis A10, Darmstadt, Germany).

3.2. Photocatalysts Synthesis

The synthesis was done by a sol-gel method [14]. Briefly, the sol was composed of TEOS, iPrOH , and water at a molar rate of 1:4:10; the homogeneous solution was changed in acid pH with 100 μL of HCl (1 M) and kept at 60 °C for 1 h, later a change to basic pH was performed with 100 μL of NH_4OH (0.6 M), the sol was then maintained at 60 °C by 6 h in a furnace until gel formation (named XGS). For metal incorporation, two methods were used. The metal was incorporated by impregnation, placing the gel in a 25 mL solution of FeCl_3 (0.1, 0.2, or 0.4 M) for 3 days with constant agitation (named XGS-Fe-Im-X.X). As an alternative, the metal was incorporated by polymerization, it was incorporated in the sol stage diluted in the water (named XGS-Fe-Pol-X.X), and two molar rate metal to silica were explored, either 1:10 (0.1) or 1:3 (0.3). The materials were washed three times with iPrOH and another three with water. The drying of all the materials was performed at 60 °C for 3 days. Every batch in XGS synthesis started with 29 mmol of TEOS, yielding a final mass around of 1.6 g for the synthesized material. Afterward, all materials were ground and sieved, and classified into three sizes: between 0.5 and 0.25 mm (L), between 0.25 and 0.1 (M), and smaller than 0.1 (S).

3.3. Photocatalyst Characterization

The surface area and the average pore size were obtained through nitrogen physisorption at 77 K in Micrometrics ASAP 2020 equipment, where the samples were previously degasified under vacuum, for 24 h at 95 °C. The BET model was used to obtain the surface area of the materials. The surface morphology was observed by scanning electron microscopy (SEM) and energy dispersive X-ray spectroscopy (EDX) using a FEI Quanta650F (Austin, TX, USA) equipment. A Mettler-Toledo model DSC-1 (Greifensee, Switzerland) equipment was used for the thermogravimetric analysis (TGA).

Crystallinity measurements were performed using X-ray diffractometry (XRD) in a Bruker D9 Discover (Madrid, Spain) equipment. The surface functional groups were observed using Fourier Transformed Infrared Spectroscopy (FTIR), JASCO 6200 (Tokyo, Japan), and Raman spectroscopy JASCO NRS-5100 (Tokyo, Japan). The surface composition was acquired via X-ray photoelectronic spectroscopy (XPS) with a PHI 5000 VersaProbe II equipment (Chanhassen, MN, USA)

Electrical properties were analyzed using diffuse reflectance spectroscopy (DRS) using the UV-Vis-NIR equipment (VARIAN model CARY-5E, Santa Clara, CA, USA). Photoluminescence spectra (PL) were measured at room temperature on a HORIBA QM-8000

fluorescence spectrometer (Kyoto, Japan) using a Xe lamp with an excitation wavelength of 380 nm.

3.4. Pharmaceuticals Degradation Tests

The photocatalysis process was performed in batch mode using quartz tubes of 2 cm in diameter in a semi-horizontal position with constant agitation. The solar radiation was provided by a simulator (Neurtek Solarbox 1500) set at 450 W/m² light intensity. All tests started with a C₀ of 15 ppm and with the S size of particles, unless specified. A period of 30 min in the dark was used to calculate adsorption, followed by a 60-min process under solar light where samples were collected at regular times, and analyzed by HPLC.

To analyze the degradation mechanism several scavengers were used: tert-Butanol (tBuOH) as a HO• radical scavenger, thiourea which acts as a scavenger for HO•, e_{aq}⁻, and H•, and NO₃⁻ that mainly inhibits the e_{aq}⁻ effect. The experiment was prepared, as usual, adding the scavenger substance to reach a concentration of 0.1 M in the solution.

HPLC was performed in a Thermo Fisher equipment (Santa Clara, CA, USA) coupled with a UV-Vis detector. An inverse-phase isocratic method was developed, using a flow rate of 0.35 mL/min, with a C-18 column (particle size of 2.6 μm; 4.6 × 150 mm) of the Phenomenex Kinetex brand. The injection volume was 50 μL. The mobile phase consisted of DW acidified with 0.1% v/v formic acid and acetonitrile on a volume ratio reported in the literature [32,40,45–47].

3.5. Kinetic Models

Two kinetic models were used to describe the degradation curves. The first-order kinetic model which is represented by the following equation:

$$-\frac{d\varphi_A}{dt} = k_1\varphi_A \quad (1)$$

where $\varphi_A = \frac{C_A}{C_0}$; C_A and C₀ are the concentrations at a certain time and at time zero, respectively, in ppm; t is time expressed in minutes; and k₁ is the first-order kinetic constant (min⁻¹). The first-order kinetic model with two parameters [31]:

$$-\frac{d\varphi_A}{dt} = k_2(\varphi_A - \beta_A) \quad (2)$$

where β_A is an adimensional adjustment parameter; and k₂ is the kinetic constant (min⁻¹). The parameter estimation was performed using a non-linear adjustment, minimizing the squared error using the Statistica software package.

To evaluate the fit from the model to the experimental data the deviation percentage was obtained by the following equation:

$$\%D = \frac{1}{N} \sum_{N=1}^N \left| \frac{q_{exp} - q_{cal}}{q_{exp}} \right| \times 100 \quad (3)$$

4. Conclusions

The characterization of the materials demonstrated that the iron salts through impregnation as well as polymerization led to a decrease in the band gap energy to achieve around 3 eV. On the other hand, PL study suggests that the recombination time of the electron-hole pair is longer for the materials doped through impregnation. On the other hand, the photodegradation test using the synthesized materials indicates that pristine XGS does not have any photocatalytic activity, similar to the XGS-Fe-Pol materials. By contrast, the materials doped through impregnation presented an important degradation activity. Using the characterization as a basis it can be deduced that the main difference is the recombination time for the electron-hole pair. It was also demonstrated that photodegradation occurs due to the generation of hydroxyl radicals in the aqueous medium.

However, when studying the reuse capabilities of the XGS-Fe-Im it was observed that the kinetic degradation constant decreased by up to 99% with respect to the first cycle, more characterization studies suggest this is due to a loss in surface iron, as well as a decrease in the recombination time of the electron-hole pair. This conducts to the knowledge that the synthesized XGS-Fe-Im material acts as a photopromoter of hydroxyl radicals rather than a true photocatalyst.

Finally, the material was tested in the degradation of the pharmaceutical compounds RNT and CIP, discovering that the degradation rate is affected by the structural complexity of the pollutant.

Supplementary Materials: The following supporting information can be downloaded at: <https://www.mdpi.com/article/10.3390/catal12111341/s1>. Figure S1: Digital photographs obtained for (a) XGS; (b) XGS-Fe-Im-0.4; and (c) XGS-Fe-Pol-0.3. Figure S2: EDX spectra obtained for (a) XGS; (b) XGS-Fe-Im-0.4; (c) XGS-Fe-Pol-0.1; and (d) XGS-Fe-Pol-0.3. Figure S3: High-resolution XPS spectra for XGS-Fe-Im-0.4 and XGS-Fe-Pol-0.3 (a) Si 2p; and (b) Fe 2p. Figure S4: Photoluminescence emission spectra for (a) XGS-Fe-Im-0.2 and 0.4; and (b) XGS-Fe-Pol-0.1 and 0.3. Figure S5: Band structure energy for several studied materials. Figure S6: (a) Micrograph and (b) EDX spectra obtained for the material XGS-Fe-Im-0.2-O. Table S1: Iron concentration in the solution measured by atomic absorption spectroscopy, a load of 1 g/L of material was used.

Author Contributions: Conceptualization, M.S.P. and J.J.S.-R.; methodology, C.B.G.-R.; validation, V.C.R., J.J.S.-R. and M.S.P.; formal analysis, C.B.G.-R.; investigation, C.B.G.-R. and V.C.R.; resources, M.S.P.; writing—original draft preparation, C.B.G.-R.; writing—review and editing, V.C.R., J.J.S.-R. and M.S.P.; visualization, C.B.G.-R. and V.C.R.; supervision, V.C.R.; project administration, V.C.R.; funding acquisition, M.S.P. All authors have read and agreed to the published version of the manuscript.

Funding: This research was funded by Junta de Andalucía and Fondo Europeo de Desarrollo Regional (FEDER) Ref. P18-RT-4193. C. García-Reyes would like to thank the scholarship fund by the Mexican National Council for Science and Technology (CONACyT) through the CVU 49215.

Data Availability Statement: Not applicable.

Conflicts of Interest: The authors declare no conflict of interest. The funders had no role in the design of the study; in the collection, analyses, or interpretation of data; in the writing of the manuscript; or in the decision to publish the results.

References

1. aus der Beek, T.; Weber, F.-A.A.; Bergmann, A.; Hickmann, S.; Ebert, I.; Hein, A.; Küster, A. Pharmaceuticals in the Environment—Global Occurrences and Perspectives. *Environ. Toxicol. Chem.* **2016**, *35*, 823–835. [[CrossRef](#)] [[PubMed](#)]
2. Alfonso-Muniozgueren, P.; Serna-Galvis, E.A.; Bussemaker, M.; Torres-Palma, R.A.; Lee, J. A Review on Pharmaceuticals Removal from Waters by Single and Combined Biological, Membrane Filtration and Ultrasound Systems. *Ultrason. Sonochem.* **2021**, *76*, 105656. [[CrossRef](#)] [[PubMed](#)]
3. Patel, M.; Kumar, R.; Kishor, K.; Mlsna, T.; Pittman, C.U.; Mohan, D. Pharmaceuticals of Emerging Concern in Aquatic Systems: Chemistry, Occurrence, Effects, and Removal Methods. *Chem. Rev.* **2019**, *119*, 3510–3673. [[CrossRef](#)] [[PubMed](#)]
4. Dey, S.; Bano, F.; Malik, A. Pharmaceuticals and Personal Care Product (PPCP) Contamination—A Global Discharge Inventory. In *Pharmaceuticals and Personal Care Products: Waste Management and Treatment Technology*; Elsevier: Amsterdam, The Netherlands, 2019; pp. 1–26. ISBN 9780128161890.
5. Tenorio-Chávez, P.; Cerro-López, M.; Castro-Pastrana, L.I.; Ramírez-Rodrigues, M.M.; Orozco-Hernández, J.M.; Gómez-Oliván, L.M. Effects of Effluent from a Hospital in Mexico on the Embryonic Development of Zebrafish, *Danio Rerio*. *Sci. Total Environ.* **2020**, *727*, 138716. [[CrossRef](#)] [[PubMed](#)]
6. Kostich, M.S.; Flick, R.W.; Batt, A.L.; Mash, H.E.; Boone, J.S.; Furlong, E.T.; Kolpin, D.W.; Glassmeyer, S.T. Aquatic Concentrations of Chemical Analytes Compared to Ecotoxicity Estimates. *Sci. Total Environ.* **2017**, *579*, 1649–1657. [[CrossRef](#)] [[PubMed](#)]
7. Berezina, N.A.; Sharov, A.N.; Chernova, E.N.; Malysheva, O.A. Effects of Diclofenac on the Reproductive Health, Respiratory Rate, Cardiac Activity, and Heat Tolerance of Aquatic Animals. *Environ. Toxicol. Chem.* **2022**, *41*, 677–686. [[CrossRef](#)]
8. García-Reyes, C.B.; Salazar-Rábago, J.J.; Sánchez-Polo, M.; Loredó-Cancino, M.; Leyva-Ramos, R. Ciprofloxacin, Ranitidine, and Chlorphenamine Removal from Aqueous Solution by Adsorption. Mechanistic and Regeneration Analysis. *Environ. Technol. Innov.* **2021**, *24*, 102060. [[CrossRef](#)]

9. Ávila, C.; García-Galán, M.J.; Uggetti, E.; Montemurro, N.; García-Vara, M.; Pérez, S.; García, J.; Postigo, C. Boosting Pharmaceutical Removal through Aeration in Constructed Wetlands. *J. Hazard. Mater.* **2021**, *412*, 125231. [[CrossRef](#)]
10. Jain, M.; Mudhoo, A.; Ramasamy, D.L.; Najafi, M.; Usman, M.; Zhu, R.; Kumar, G.; Shobana, S.; Garg, V.K.; Sillanpää, M. Adsorption, Degradation, and Mineralization of Emerging Pollutants (Pharmaceuticals and Agrochemicals) by Nanostructures: A Comprehensive Review. *Environ. Sci. Pollut. Res.* **2020**, *27*, 34862–34905. [[CrossRef](#)]
11. Chen, W.-H.; Wong, Y.-T.; Huang, T.-H.; Chen, W.-H.; Lin, J.-G. Removals of Pharmaceuticals in Municipal Wastewater Using a Staged Anaerobic Fluidized Membrane Bioreactor. *Int. Biodeterior. Biodegrad.* **2019**, *140*, 29–36. [[CrossRef](#)]
12. Khan, A.H.; Khan, N.A.; Ahmed, S.; Dhingra, A.; Singh, C.P.; Khan, S.U.; Mohammadi, A.A.; Changani, F.; Yousefi, M.; Alam, S.; et al. Application of Advanced Oxidation Processes Followed by Different Treatment Technologies for Hospital Wastewater Treatment. *J. Clean. Prod.* **2020**, *269*, 122411. [[CrossRef](#)]
13. Mirzaei, A.; Chen, Z.; Haghghat, F.; Yerushalmi, L. Removal of Pharmaceuticals and Endocrine Disrupting Compounds from Water by Zinc Oxide-Based Photocatalytic Degradation: A Review. *Sustain. Cities Soc.* **2016**, *27*, 407–418. [[CrossRef](#)]
14. Acosta-Rangel, A.; Sánchez-Polo, M.; Polo, A.M.S.; Rivera-Utrilla, J.; Berber-Mendoza, M.S. Tinidazole Degradation Assisted by Solar Radiation and Iron-Doped Silica Xerogels. *Chem. Eng. J.* **2018**, *344*, 21–33. [[CrossRef](#)]
15. el mehdi Benacherine, M.; Debbache, N.; Ghoul, I.; Mameri, Y. Heterogeneous Photoinduced Degradation of Amoxicillin by Goethite under Artificial and Natural Irradiation. *J. Photochem. Photobiol. A Chem.* **2017**, *335*, 70–77. [[CrossRef](#)]
16. Velo-Gala, I.; López-Peñalver, J.J.; Sánchez-Polo, M.; Rivera-Utrilla, J. Comparative Study of Oxidative Degradation of Sodium Diatrizoate in Aqueous Solution by $\text{H}_2\text{O}_2/\text{Fe}^{2+}$, $\text{H}_2\text{O}_2/\text{Fe}^{3+}$, Fe (VI) and UV, $\text{H}_2\text{O}_2/\text{UV}$, $\text{K}_2\text{S}_2\text{O}_8/\text{UV}$. *Chem. Eng. J.* **2014**, *241*, 504–512. [[CrossRef](#)]
17. Shi, L.; Yang, L.; Zhang, H.; Chang, K.; Zhao, G.; Kako, T.; Ye, J. Implantation of Iron(III) in Porphyrinic Metal Organic Frameworks for Highly Improved Photocatalytic Performance. *Appl. Catal. B Environ.* **2018**, *224*, 60–68. [[CrossRef](#)]
18. Shelton, T.L.; Bensema, B.L.; Brune, N.K.; Wong, C.; Yeh, M.; Osterloh, F.E. Photocatalytic Water Oxidation with Iron Oxide Hydroxide (Rust) Nanoparticles. *J. Photonics Energy* **2016**, *7*, 012003. [[CrossRef](#)]
19. Andrade-Espinosa, G.; Escobar-Barrios, V.; Rangel-Mendez, R. Synthesis and Characterization of Silica Xerogels Obtained via Fast Sol–Gel Process. *Colloid Polym. Sci.* **2010**, *288*, 1697–1704. [[CrossRef](#)]
20. Çok, S.S.; Koç, F.; Balkan, F.; Gizli, N. Exploring a New Preparation Pathway for the Synthesis of Silica Based Xerogels as Crack-Free Monoliths. *Ceram. Int.* **2019**, *45*, 1616–1626. [[CrossRef](#)]
21. Hernández-Campos, M.; Polo, A.M.S.; Sánchez-Polo, M.; Rivera-Utrilla, J.; Berber-Mendoza, M.S.; Andrade-Espinosa, G.; López-Ramón, M.V. Lanthanum-Doped Silica Xerogels for the Removal of Fluorides from Waters. *J. Environ. Manag.* **2018**, *213*, 549–554. [[CrossRef](#)]
22. Wang, R.; Ng, D.H.L.; Liu, S. Recovery of Nickel Ions from Wastewater by Precipitation Approach Using Silica Xerogel. *J. Hazard. Mater.* **2019**, *380*, 120826. [[CrossRef](#)] [[PubMed](#)]
23. Morosanova, M.A.; Chaikun, K.V.; Morosanova, E.I. Silica and Silica–Titania Xerogels Doped with Iron(III) for Total Antioxidant Capacity Determination. *Materials* **2021**, *14*, 2019. [[CrossRef](#)] [[PubMed](#)]
24. Rebbouh, L.; Rosso, V.; Renotte, Y.; Lion, Y.; Grandjean, F.; Heinrichs, B.; Pirard, J.P.; Delwiche, J.; Hubin-Franskin, M.J.; Long, G.J. The Nonlinear Optical, Magnetic, and Mössbauer Spectral Properties of Some Iron(III) Doped Silica Xerogels. *J. Mater. Sci.* **2006**, *41*, 2839–2849. [[CrossRef](#)]
25. Fatimah, I.; Prakoso, N.I.; Sahroni, I.; Musawwa, M.M.; Sim, Y.L.; Kooli, F.; Muraza, O. Physicochemical Characteristics and Photocatalytic Performance of $\text{TiO}_2/\text{SiO}_2$ Catalyst Synthesized Using Biogenic Silica from Bamboo Leaves. *Heliyon* **2019**, *5*, e02766. [[CrossRef](#)]
26. Chen, Q.; Shi, H.; Shi, W.; Xu, Y.; Wu, D. Enhanced Visible Photocatalytic Activity of Titania–Silica Photocatalysts: Effect of Carbon and Silver Doping. *Catal. Sci. Technol.* **2012**, *2*, 1213–1220. [[CrossRef](#)]
27. Andrade Espinosa, G. Síntesis De Xerogeles De Sílice Como Soporte De Partículas De Hidro(Óxidos) De Hierro Para La Adsorción De Arsénico Presente En Solución Acuosa. Doctoral Thesis, Repositorio IPICYT, San Luis Potosí S.L.P., México, 2011.
28. Barczak, M. Amine-Modified Mesoporous Silicas: Morphology-Controlled Synthesis toward Efficient Removal of Pharmaceuticals. *Microporous Mesoporous Mater.* **2019**, *278*, 354–365. [[CrossRef](#)]
29. Das, S.; Hendry, M.J. Application of Raman Spectroscopy to Identify Iron Minerals Commonly Found in Mine Wastes. *Chem. Geol.* **2011**, *290*, 101–108. [[CrossRef](#)]
30. Fu, H.; Ding, X.; Ren, C.; Li, W.; Wu, H.; Yang, H. Preparation of Magnetic Porous $\text{NiFe}_2\text{O}_4/\text{SiO}_2$ Composite Xerogels for Potential Application in Adsorption of Ce(IV) Ions from Aqueous Solution. *RSC Adv.* **2017**, *7*, 16513–16523. [[CrossRef](#)]
31. Ocampo-Pérez, R.; Sánchez-Polo, M.; Rivera-Utrilla, J.; Leyva-Ramos, R. Enhancement of the Catalytic Activity of TiO_2 by Using Activated Carbon in the Photocatalytic Degradation of Cytarabine. *Appl. Catal. B Environ.* **2011**, *104*, 177–184. [[CrossRef](#)]
32. Wang, L.; Yang, J.; Li, Y.; Lv, J.; Zou, J. Removal of Chlorpheniramine in a Nanoscale Zero-Valent Iron Induced Heterogeneous Fenton System: Influencing Factors and Degradation Intermediates. *Chem. Eng. J.* **2016**, *284*, 1058–1067. [[CrossRef](#)]
33. Mar-Ortiz, A.F.; Salazar-Rábago, J.J.; Sánchez-Polo, M.; Rozalen, M.; Cerino-Córdova, F.J.; Loredó-Cancino, M. Photodegradation of Antihistamine Chlorpheniramine Using a Novel Iron-Incorporated Carbon Material and Solar Radiation. *Environ. Sci. Water Res. Technol.* **2020**, *6*, 2607–2618. [[CrossRef](#)]

34. López-Velázquez, K.; Guzmán-Mar, J.L.; Montalvo-Herrera, T.J.; Mendiola-Alvarez, S.Y.; Villanueva-Rodríguez, M. Efficient Photocatalytic Removal of Four Endocrine-Disrupting Compounds Using N-Doped BiOBr Catalyst under UV-Vis Radiation. *J. Environ. Chem. Eng.* **2021**, *9*, 106185. [[CrossRef](#)]
35. Kamarulzaman, N.; Kasim, M.F.; Chayed, N.F. Elucidation of the Highest Valence Band and Lowest Conduction Band Shifts Using XPS for ZnO and Zn_{0.99}Cu_{0.01}O Band Gap Changes. *Results Phys.* **2016**, *6*, 217–230. [[CrossRef](#)]
36. Wu, D.; Yue, S.; Wang, W.; An, T.; Li, G.; Ye, L.; Yip, H.Y.; Wong, P.K. Influence of Photoinduced Bi-Related Self-Doping on the Photocatalytic Activity of BiOBr Nanosheets. *Appl. Surf. Sci.* **2017**, *391*, 516–524. [[CrossRef](#)]
37. Chang, F.; Li, C.; Chen, J.; Wang, J.; Luo, J.; Xie, Y.; Deng, B.; Hu, X. Enhanced Photocatalytic Performance of G-C₃N₄ Nanosheets–BiOBr Hybrids. *Superlattices Microstruct.* **2014**, *76*, 90–104. [[CrossRef](#)]
38. Zhang, B.; Fu, S.; Wang, D.; Jiao, S.; Zeng, Z.; Zhang, X.; Xu, Z.; Liu, Y.; Zhao, C.; Pan, J.; et al. Synthesis and Enhanced Light Photocatalytic Activity of Modulating Band BiOBrXII–X Nanosheets. *Nanomaterials* **2021**, *11*, 2940. [[CrossRef](#)] [[PubMed](#)]
39. Salazar-Rábago, J.J.; Sánchez-Polo, M.; Rivera-Utrilla, J.; Leyva-Ramos, R.; Ocampo-Pérez, R.; Carrasco-Marin, F. Organic Xerogels Doped with Tris (2,2'-Bipyridine) Ruthenium(II) as Hydroxyl Radical Promoters: Synthesis, Characterization, and Photoactivity. *Chem. Eng. J.* **2016**, *306*, 289–297. [[CrossRef](#)]
40. Radjenović, J.; Sirtori, C.; Petrović, M.; Barceló, D.; Malato, S. Characterization of Intermediate Products of Solar Photocatalytic Degradation of Ranitidine at Pilot-Scale. *Chemosphere* **2010**, *79*, 368–376. [[CrossRef](#)]
41. Zou, X.; Zhang, J.; Zhao, X.; Zhang, Z. MoS₂/RGO Composites for Photocatalytic Degradation of Ranitidine and Elimination of NDMA Formation Potential under Visible Light. *Chem. Eng. J.* **2020**, *383*, 123084. [[CrossRef](#)]
42. Zheng, X.; Xu, S.; Wang, Y.; Sun, X.; Gao, Y.; Gao, B. Enhanced Degradation of Ciprofloxacin by Graphitized Mesoporous Carbon (GMC)-TiO₂ Nanocomposite: Strong Synergy of Adsorption-Photocatalysis and Antibiotics Degradation Mechanism. *J. Colloid Interface Sci.* **2018**, *527*, 202–213. [[CrossRef](#)]
43. Núñez-Salas, R.E.; Hernández-Ramírez, A.; Santos-Lozano, V.; Hinojosa-Reyes, L.; Guzmán-Mar, J.L.; Gracia-Pinilla, M.Á.; de Lourdes Maya-Treviño, M. Synthesis, Characterization, and Photocatalytic Performance of FeTiO₃/ZnO on Ciprofloxacin Degradation. *J. Photochem. Photobiol. A Chem.* **2021**, *411*, 113186. [[CrossRef](#)]
44. Wade, L.G. *Organic Chemistry*; New in Organic Chemistry Series; Prentice Hall PTR: Hoboken, NJ, USA, 2011; ISBN 9780321768148.
45. Olvera-Vargas, H.; Oturan, N.; Oturan, M.A.; Brillas, E. Electro-Fenton and Solar Photoelectro-Fenton Treatments of the Pharmaceutical Ranitidine in Pre-Pilot Flow Plant Scale. *Sep. Purif. Technol.* **2015**, *146*, 127–135. [[CrossRef](#)]
46. Haddad, T.; Kümmerer, K. Characterization of Photo-Transformation Products of the Antibiotic Drug Ciprofloxacin with Liquid Chromatography-Tandem Mass Spectrometry in Combination with Accurate Mass Determination Using an LTQ-Orbitrap. *Chemosphere* **2014**, *115*, 40–46. [[CrossRef](#)] [[PubMed](#)]
47. Durán-Álvarez, J.C.; Avella, E.; Ramírez-Zamora, R.M.; Zanella, R. Photocatalytic Degradation of Ciprofloxacin Using Mono- (Au, Ag and Cu) and Bi- (Au–Ag and Au–Cu) Metallic Nanoparticles Supported on TiO₂ under UV-C and Simulated Sunlight. *Catal. Today* **2016**, *266*, 175–187. [[CrossRef](#)]